High-speed unsteady flows around spiked-blunt bodies

ARGYRIS G. PANARAS† AND DIMITRIS DRIKAKIS

Department of Aerospace Sciences, Cranfield University, Cranfield MK43 0AL, UK

This paper presents a detailed investigation of unsteady supersonic and hypersonic flows around spiked-blunt bodies, including the investigation of the effects of the flow field initialization on the flow results. Past experimental research has shown that if the geometry of a spiked-blunt body is such that a shock formation consisting of an oblique foreshock and a bow aftershock appears, then the flow may be unsteady. The unsteady flow is characterized by periodic radial inflation and collapse of the conical separation bubble formed around the spike (pulsation). Beyond a certain spike length the flow is 'stable', i.e. steady or mildly oscillating in the radial direction. Both unsteady and 'stable' conditions have been reported when increasing or decreasing the spike length during an experimental test and, additionally, hysteresis effects have been observed. The present study reveals that for certain geometries the numerically simulated flow depends strongly on the assumed initial flow field, including the occurrence of bifurcations due to inherent hysteresis effects and the appearance of unsteady flow modes. Computations using several different configurations reveal that the transient (initial) flow development corresponds to a nearly inviscid flow field characterized by a foreshock–aftershock interaction. When the flow is pulsating, the further flow development is not sensitive to initial conditions, whereas for an oscillating or almost 'steady' flow, the flow development depends strongly on the assumed initial flow field.

---

1. Introduction

Shock waves and shock–shock interactions appearing around air vehicles flying at supersonic or hypersonic speeds often lead to high localized temperatures and associated extremely high heating rates on the surface of the vehicle. The severe damage of the ventral fin of the X-15 experimental hypersonic vehicle during a Mach 6.7 high-altitude flight in 1967 is a classical example of adverse effect of shock–shock interactions. Typical shock–shock interactions around a re-entry vehicle are shown in figure 1 (Schramm & Eitelberg 1999).

The various possible patterns of shock–shock interactions have been studied experimentally by Edney (1968). He studied the effect of a weak oblique shock wave impingement at various radial positions on the bow shock that envelops a hemisphere–cylinder at hypersonic speed. Six types of shock–shock interactions were identified, with the so-called type III and IV patterns being well known for their detrimental effects. Type III interactions feature a shear layer and Type IV interactions feature a

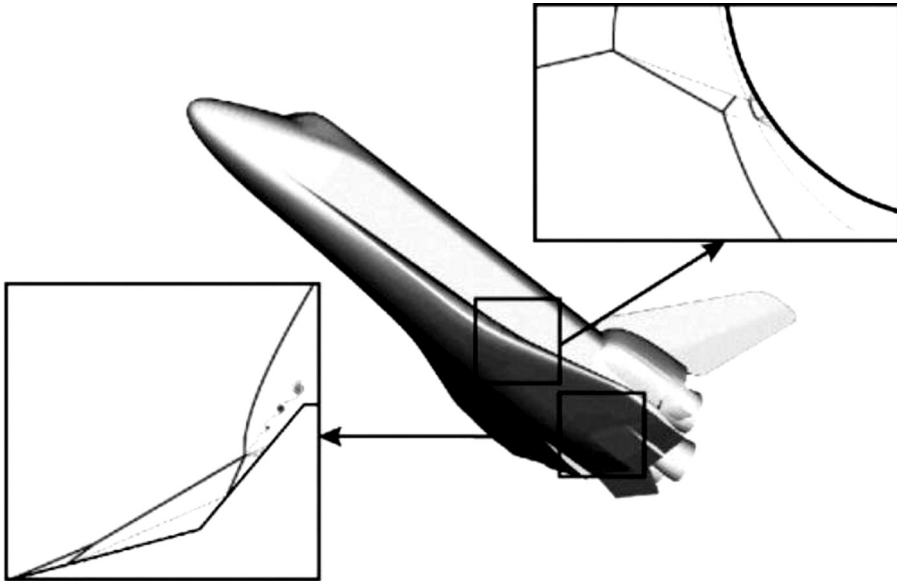† E-mail address for correspondence: a.panaras@cranfield.ac.uk

FIGURE 1. Schematic presentation of foreshock–aftershock interactions around a re-entry vehicle (Schramm 1999).

supersonic jet at the shock intersection point with high heating rates (and pressure) at the region of their impingement on the surface of the body.

The spiked-blunt bodies are typical configurations associated with shock–shock interactions. Various shapes of these bodies are used in a variety of applications in aeronautics, including axisymmetric jet inlets with conical centrebody; ballistic missiles drag reduction by spike; plasma or hot gas injection; parachutes for pilot-ejection capsules; and ablation associated with re-entry problems (Feszty, Badcock & Richards 2004*a*, *b*). In addition, cone-flare, double cones and hollow cylinder-flare are alternative configurations used to study the flow structure around control surfaces and to validate computational methods and computer codes (e.g. Holden *et al.* 2002).

Past experimental and computational investigations of unsteady flows around spiked-blunt bodies have almost exclusively employed the spiked cylinder geometry as a generic model configuration. The cylinder may be flat-ended or have a conical or hemispherical cap. The interest in spiked bodies has its origin in the effort to compromise two desired but non-similar characteristics of re-entry bodies; a large nose radius for the re-entry phase (low heat transfer), and a pointed nose (low drag) for the atmospheric flight phase. The presence of a variable length spike protruding from the stagnation point of an axially symmetric blunt body provides at least a partial solution. From the early 1950s to the 1980s, numerous studies have been performed for this configuration. The experimental work of Mair (1952), Wood (1960), Maull (1962) and Kabelitz (1971) has provided valuable information regarding the structure, classification and boundaries of the unsteady flows.

One critical feature of the flow around spiked bodies is the unsteadiness that occurs for certain combinations of the ratio of the spike length to body diameter and the shape of the body, provided that the body alone causes a detached shock wave (Wood 1960). Kabelitz (1971) has found two distinct instability modes, illustrated in figure 2 by the experimental data of Panaras (1976). These results are for the laminar flow around a spiked flat-ended cylinder at Mach number, $M = 6.0$, and Reynolds
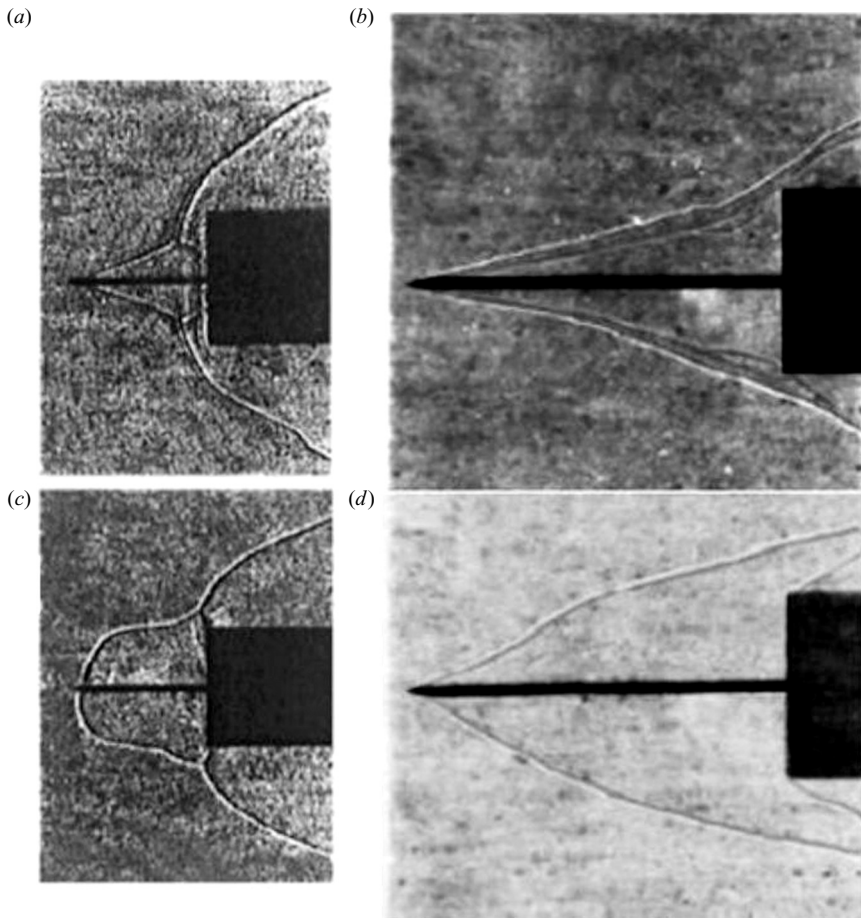
FIGURE 2. (a, c) Pulsation mode around a spiked cylinder ($M = 6.0$, $L/D = 1.0$); (b, d) oscillation mode around a spiked cylinder ($M = 6.0$, $L/D = 2.0$) (Panaras 1976).

number $Re = 1.3 \times 10^5$, based on the free stream velocity and blunt body diameter; this Reynolds number definition is used throughout the paper. Figure 2(a, c) shows the 'pulsation' mode where the conical separation bubble formed on the concave part of the body periodically inflates and radially expands, taking a hemispherical shape. In the 'oscillation' mode (figure 2b, d), the unsteadiness is milder; the conical foreshock, which envelops the separation bubble, and the accompanying shear layer oscillate laterally and their shape changes periodically from concave to convex.

The oscillating flow around a spiked cylinder is a subclass of the self-sustained oscillations of impinging free shear layers (cavities, edge tone). Thus, the driving mechanism of the oscillation is related to effect of the pressure perturbations generated at the impingement surface on the stability of the shear layer (Panaras 1985), which envelops the conical separation bubble.

However, the mechanism of the pulsation is quite different. Various hypotheses have been proposed for the driving mechanism of the pulsation mode. Panaras (1976) was the first to suggest that the pulsation is due to the effect of the annular supersonic jet – appearing at the foreshock/aftershock intersection – on the initially conical separation bubble. Panaras (1976, 1981) also observed that the related
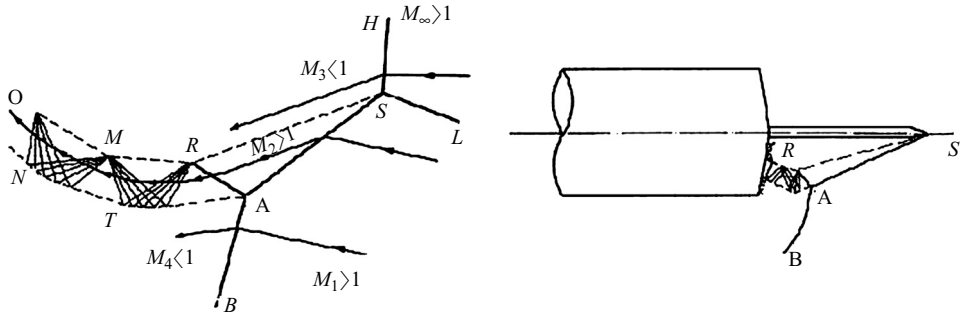
FIGURE 3. The generation of the supersonic jet. Similarity with Edney's type VI shock formation (Panaras 1976).

shock–shock interaction is the unsteady counterpart of that classified by Edney as type IV interaction (Edney 1968), also shown schematically in figure 3. Since the supersonic jet is curved towards the body axis (figure 2*a*), it directs the high pressure air from the region behind the conical foreshock into the dead-air region, thereby inducing its inflation and radial expansion. Due to the radial expansion (figure 2*c*), the shock intersection point moves away from the body. Subsequently, the separation bubble collapses downstream since there is no disturbance to sustain it. This leads to the establishment of the initial conditions of impulsive flow, i.e. the body is exposed to free stream conditions. Then a new unsteady-flow cycle starts again. More recently, Feszty *et al.* (2004*a*) improved significantly the flow model proposed by Panaras (1976) and provided more details of the instability mechanism. They observed the occurrence of a separation vortex and showed that the air which inflates the separation bubble does not originate from the annular supersonic jet, but comes from the bubble itself where it is trapped during the early stage of each unsteady-flow cycle.

According to experimental evidence, if during a series of tests the spike length is changed outside the wind tunnel and the experiment is repeated, the shift from the pulsation to the oscillation mode appears abruptly at a particular spike length. However, if the spike length changes during a run within the wind tunnel, a hysteresis phenomenon occurs. This is well visualized and described by Calarese & Hankey (1985), in their $M = 3.0$, Reynolds number 3.94×10^5 experiments on a cone-frustum axisymmetric model equipped with a retractable spike. When the spike was retracted during the experiments, hysteresis was detected (see figure 4), which was attributed to the fact that the shock configuration tends to conserve its state. Once the pulsation mode is induced by the spike's outward motion, it sustains itself even when the spike reaches a length which would require the beginning of the stable configuration (indicated by low levels of pressure fluctuations). Similarly, when the spike is retracted, the existing stable shock configuration tends to remain unchanged for spike lengths which would require the beginning of shock pulsation.

The instabilities which appear for a certain range of geometric parameters in the high-speed flows around spiked-blunt bodies can cause undesirable effects, such as severe vibration of the structure, increased heating and unsteady pressure loads. Thus, there is a strong interest in understanding the physics of these flows. Furthermore, the subject of how well numerical schemes can mimic the solution behaviour of the underlying partial differential equation (PDE) model for finite time steps and grid spacing is an area of research with wider implications on flow modelling and
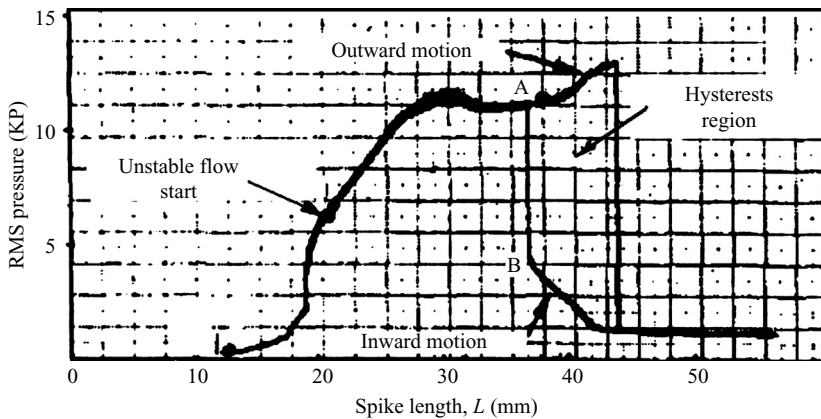
FIGURE 4. Hysteresis limits (Calarese & Hankey 1985).

scientific computing. Such issues have also been discussed by other authors in the past (Drikakis & Smolarkiewicz 2001; Yee 2001).

The aim of the present research is to elucidate the following questions: (1) What is the driving mechanism of the pulsation and oscillation instabilities? (2) What are the effects of the flow field initialization on the development of these instabilities? and (3) Can numerical simulations provide physically realizable answers with reference to wind tunnel experiments and under what initialization and geometrical conditions? Elucidation of the above questions will eventually lead to a better understanding of the flow physics in high-speed flows around spiked bodies and stimulate further research with regards to flow control approaches for passive suppression or even complete elimination of flow instabilities.

2. Description of high-speed flows and computational approach

In order to gain a comprehensive understanding of the flow physics around spiked-blunt bodies, several different cases were examined. The selection of the geometries and flow conditions was based on the following criteria: (i) the existence of experimental data (at least Schlieren pictures); (ii) the flow to be laminar, in order to avoid uncertainties associated with turbulence modelling; (iii) to cover a broad range of spiked-blunt configurations and Mach numbers; (iv) to cover a broad range of instabilities and hysteresis effects, which is not possible to be covered by a single type of experiment. For example, the VKI spiked cylinder experiments (Panaras 1976; Kenworthy 1978) revealed the existence of both pulsating and oscillating instability modes (see §3.1 for detailed discussion) without, however, providing information about the hysteresis phenomenon due to the discrete type of each wind tunnel run. On the other hand, the cone-frustum with retractable spike experiment (Calarese & Hankey 1985) enables the study of hysteresis (see §3.2 for detailed discussion). Also, the spiked hemisphere cylinder of Crawford (1959) and the conic body experiments of Panaras (1976) cover stable flow regimes. A summary of the geometries and flow conditions is given in table 1.

Computational modelling of the high-speed flows around the spiked-blunt bodies has been performed using the Navier–Stokes equations in axisymmetric form (Batchelor 2000). The governing equations are presented in the Appendix. The perfect gas equation of state has been employed with a ratio of specific heats, $\gamma = 1.4$. The

Configuration	Mach number	Reynolds number (based on blunt body diameter)	Ratio of spike length to body diameter (L/D)	Source
Spiked flat-ended cylinder	6.0	1.3×10^5	1.0, 2.0 & 2.5	Panaras (1977) Kenworthy (1978)
Cone frustrum with retractable Spike	3.0	3.94×10^5	0.8	Calarese & Hankey (1985)
Spiked hemisphere cylinder	6.8	1.4×10^5 2.3×10^5	0.5 0.5	Crawford (1959)
Conic bodies	6.0	1.2×10^5	–	Panaras (1977)

TABLE 1. Configurations considered in the present study.

equations have been written in curvilinear body-fitted grid co-ordinates (see, for example, Drikakis & Rider 2005 and references therein).

The solution of the equations was carried out using the computational code ISAAC, developed by Morrison (1992) at NASA Langley. A second-order upwind-biased finite-volume method was employed using Roe's approximate Riemann solver (Roe 1981) in conjunction with the MUSCL scheme of van Leer (1979). The viscous terms were discretized using a central difference scheme. An implicit spatially split diagonalized approximate factorization solver (Morrison 1992), was employed for the time integration The code can be used for second-order time-accurate computations based on two sub-iteration schemes: physical-time iteration (henceforth labelled as 't-ts') or pseudo-time iteration (henceforth labelled as 'τ-ts') (Rumsey *et al.* 1996). The physical-time iteration is based on the actual physical time step. This limits the maximum time step taken due to stability considerations of the iterative scheme. The alternative is the pseudo-time iteration, which iterates within each real time step using the local CFL value. This removes the time step restriction as the iterative process advances within its stability limits. Most of the computations in this study were carried out using the pseudo-time iteration option. Computations performed using the physical-time iteration option provided identical results. In the present study, all the examined cases concerned laminar flows, thus no turbulence model was employed in the calculations. This is similar to all previous studies performed for the same geometries and flow conditions as the ones considered here (Shang, Hankey & Smith 1980; Mehta 2002; Feszty *et al.* 2004*a*,*b*).

The effects of flow initialization conditions on the flow development were examined for two different procedures: (i) 'uniform-unsteady condition' (UUC) initializes the flow variables to a uniform flow field based on the free stream conditions and applies the unsteady flow solver from the beginning of the simulation; (ii) 'steady-feeding-unsteady' (SFU) is based on an approximate steady-state solution which is obtained by applying the steady solver; this pseudo-steady solution SFU procedure method requires smaller computation time, so the majority of the published numerical investigations related to high-speed time-dependent flows are based on computations using this method. Naturally, both methods should lead to the same results. However, in the course of this study it was discovered that in the particular case of the unsteady flows around spiked-blunt bodies, in some test cases, direct application of the unsteady solver (UUC procedure) leads to erroneous results. To the contrary, application of the SFU procedure, i.e. application initially of a steady solver, leads to physically

realizable results compared to the experiment. The details of the flow predictions are presented in the rest of the paper.

3. Results

3.1. *VKI spiked flat-ended cylinders*

The first flow configuration examined is the VKI spiked flat-ended cylinder at Mach 6.0 and Reynolds number 1.3×10^5. Three ratios of the spike length (L) to the body diameter (D) were considered: $L/D = 1.0$, 2.0 and 2.5. According to Panaras (1977), the short-spike configuration results in the pulsation mode, while the longer-spike configurations exhibit the oscillating mode. The experimental results include Schlieren images and time-dependent pressure variations at a point ($r/R = 0.5$) on the surface of the cylinder (Kenworthy 1978). Recently these flows have been studied numerically by Feszty *et al.* (2004*a*, *b*).

The present axisymmetric computations were performed using a structured grid consisting of three blocks. To eliminate numerical uncertainties, several refinement studies were performed with respect to the grid, time step and number of sub-iterations (see discussion below). Although the solutions obtained may not be strictly speaking fully grid-converged solutions, the 'fine' grid selected for each case was found to provide similar results to the grid labelled as 'medium', with respect to the unsteady cycle of flow development; position of pressure peaks and amplitudes. For the present case a mesh refinement study was carried out using three grids containing 16 381 (labelled as 'coarse'), 61 750 (medium) and 147 439 (fine) grid points with the first cell off the surface located at $10^{-3}D$. A time-step refinement was also investigated using the 'fine grid' and two time steps differing by a factor of 10; non-dimensional $dt = 0.0005$ and 0.00005 based on $dt_{real}(U_\infty/D)$ where U_∞ is the free stream velocity and D the blunt body diameter. Finally, a near-wall grid-spacing refinement using the grid containing 147 439 points and the first grid cell off the wall located at $10^{-4}D$. Both flow initializations, mentioned in §2, were considered. Results of application of the UUC are shown in figure 5 for $L/D = 1.0$. In agreement with the experimental evidence (figure 2*a*, *c*) the predicted flow is pulsating. Application of the SFU procedure to the $L/D = 1.0$ test case provided similar results, i.e. the establishment of a pulsation mode. The SFU procedure was also employed in Feszty *et al.* (2004*a*, *b*).

Results of the SFU procedure for the $L/D = 1.0$ test case are shown in figure 6. Figures 6(*a*) and 6(*b*) demonstrate the limits of the periodic flow provided by the steady solver, while figure 6(*c*) shows a snapshot of the pulsation cycle as predicted by the unsteady solver. The non-dimensional pressure variation, $p = p_{real}/(\rho_\infty U_\infty^2)$ where p_{real} is the dimensional pressure and ρ_∞ is the free stream density – at a point of the cylinder located at a radial location $r/R = 0.5$ (r is the radial distance or radius of curvature, and R is the blunt-body radius) – on the flat end of the cylinder is shown in figure 7. The above non-dimensionalization has been selected to allow comparisons with the results of Feszty *et al.* (2004*a*, *b*). The non-dimensional time is defined as $t = t_{real}(U_\infty/D)$, where t_{real} is the real time. The present results are very similar to those reported by Feszty *et al.* (2004*a*). Although there are still some discrepancies between the results obtained on the 'medium' and 'fine' grids, the pressure peaks are captured at the same times and have the same amplitude for most positions throughout the unsteady cycle. With unsteady flows, and thin viscous layers oscillating across the domain, ensuring satisfactory resolution is not straightforward. However, calculation of the error with respect to pressure peak positions and root-mean-square pressure
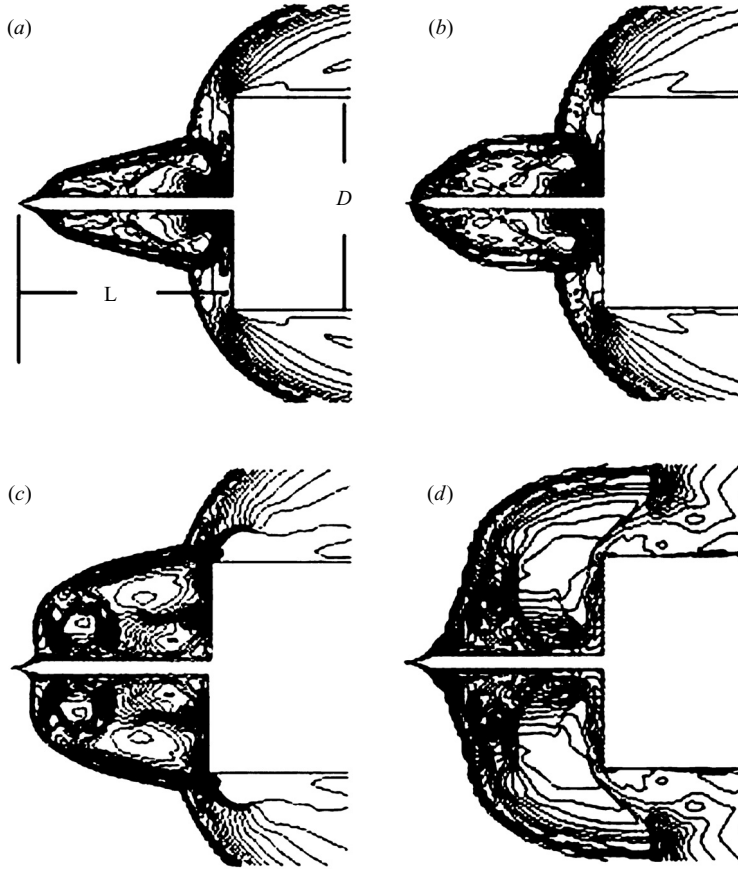
FIGURE 5. Flow solution development, (*a*) to (*d*), around the spiked cylinder for $M = 6.0$, $L/D = 1.0$. Similar solutions were obtained using the UUC and SFU procedures.

amplitudes for different grid resolutions showed that when doubling the grid cells in each direction the error is confined within a 1 %–3 % (depending on the time instant taken for estimating the error with respect to the pressure peak position).

In order to examine the effects of the flow initialization on the unsteady flow mode, the length of the spike was increased to $L/D = 2.0$ and computations were performed using both the UUC and SFU procedures. According to the experiment, for $L/D = 2.0$, the flow exhibits the oscillation mode (figure 2*b*, *d*). For the numerical simulations, UUC predicts a pulsation mode (figure 8), whereas SFU predicts an oscillating mode (figure 9), as it was also observed in the experiment. The occurrence of flow bifurcation and its dependence on initial conditions deserves further investigation because these are not simply numerical effects but are intimately related to the physical behaviour of the unstable flow in question, especially since hysteresis effects have been detected in several experimental studies.

To investigate the origin of the bifurcating behaviour, the very early stages of the flow development were examined using the UUC and SFU procedures (figures 10 and 11). Initially, both solution procedures provide similar flow behaviour, e.g. a shock system appears (figure 10*b*) and a conical separation bubble is formed (figure 11*b*). However, the SFU procedure gives a smaller bubble, especially in the upstream direction along the spike. This is due to smaller time steps near the wall which arise
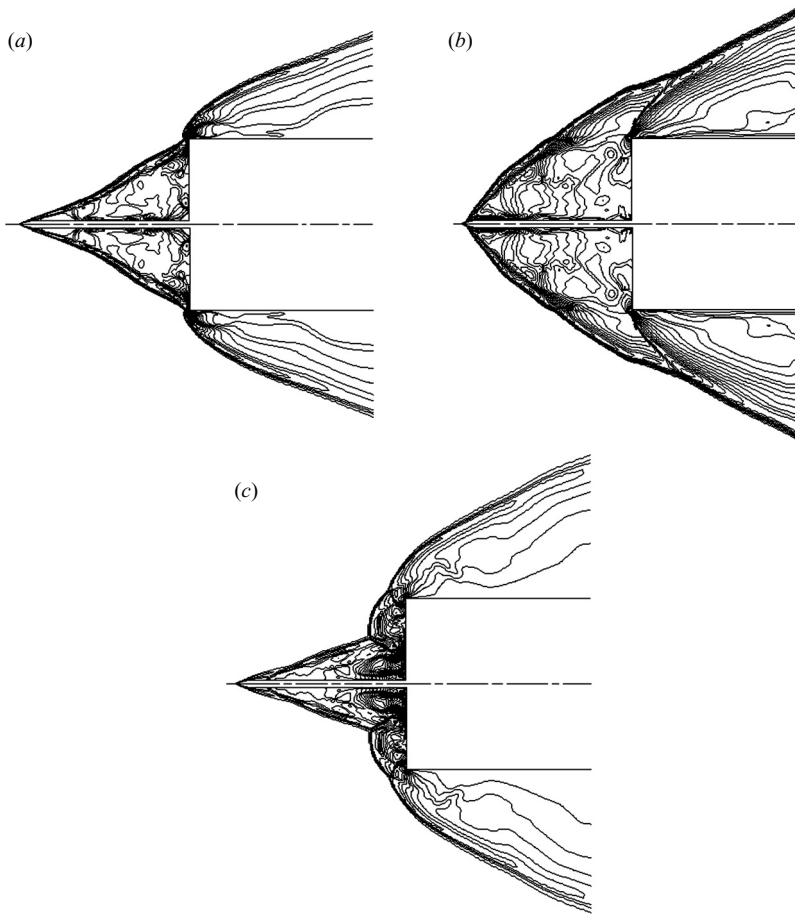
FIGURE 6. Spiked cylinder, $M = 6.0$, $L/D = 1.0$. Flow solution development for the SFU procedure; (*a*), (*b*) limits of periodic solution provided by the steady solver, (*c*) a snapshot of the pulsation cycle predicted by the unsteady solver.

from the local time steps scaling by the Jacobian as a result of the steady solver used for initialization in the SFU procedure. In the case of SFU, when the shock triple point reaches the region of the shoulder of the cylinder (figure 11*c*), the conical separation bubble hardly covers half of the available volume between the tip of the spike and the surface of the cylinder. However, the UUC procedure results in the conical separation bubble occupying the whole available volume (figure 10*c*) before the triple point reaches the shoulder of the cylinder. This difference is fundamental to further flow development.

In the case of SFU, the separation bubble communicates with the downstream expansion region (figure 11*d*) and the excess air escapes downstream, leading to the final steady-flow conditions shown in figure 11(*e*, *f*). In the case of UUC, the inflation of the bubble continues, leading to the unstable condition shown in figure 10(*d*), which cannot be sustained and collapses to the solution shown in figure 10(*e*). Noticeably, figure 10(*e*) resembles the starting condition of a pulsating flow, while figure 11(*e*, *f*) resembles an oscillating flow. Subsequent use of the above flow fields as initial flow
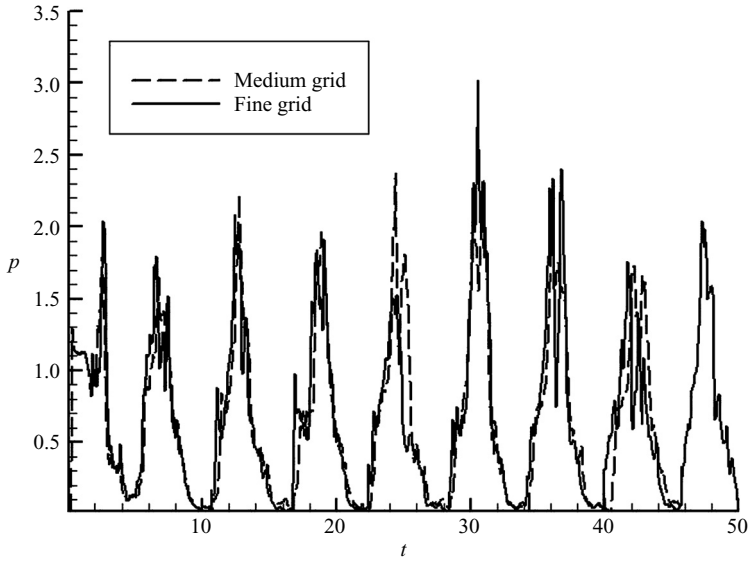
FIGURE 7. Spiked cylinder, $M = 6.0$, $L/D = 1.0$. Effect of grid resolution on pressure variations at a point on the surface of the cylinder located at radial distance from the axis, $r/R = 0.5$.
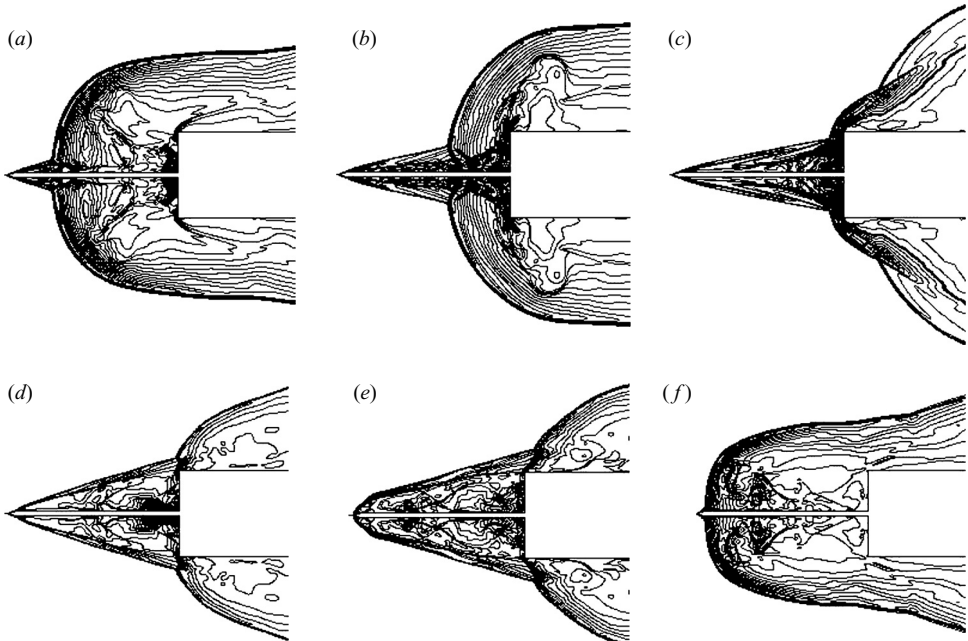

FIGURE 8. Spiked cylinder, $M = 6.0$, $L/D = 2.0$. Results using the UUC procedure.

conditions resulted in the radically different solutions shown in figures 8 and 9. The above results clearly indicate the existence of flow bifurcation depending on the initial flow conditions.
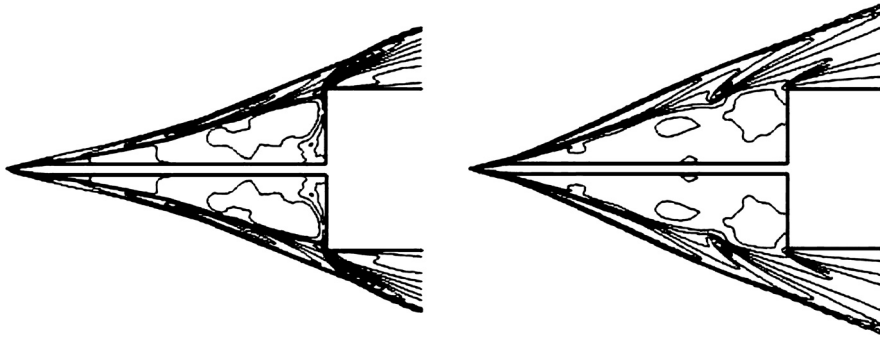
FIGURE 9. Spiked cylinder, $M = 6.0$, $L/D = 2.0$. Flow solution development for the SFU procedure.
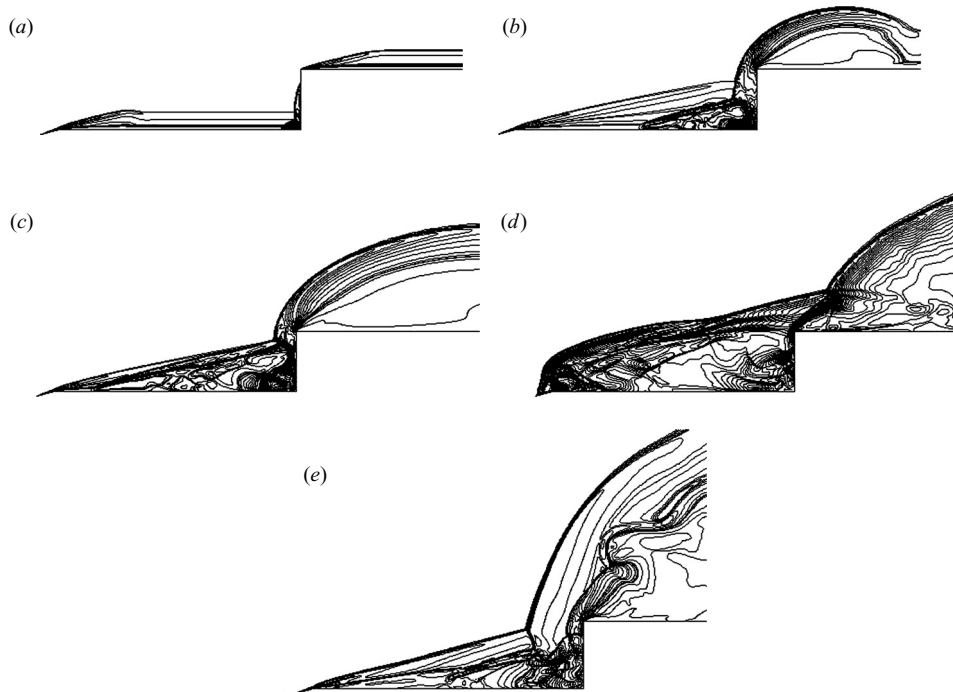
FIGURE 10. Spiked cylinder, $M = 6.0$, $L/D = 2.0$. Initial flow development obtained with the UUC procedure.

To investigate the limits of bifurcation, a configuration with a longer spike $L/D = 2.5$ was investigated using the UUC procedure. Initially, the flow development was similar to that described previously with the flow undergoing two complete pulsation cycles (not shown here). However, during the third cycle, the flow gradually started a periodic oscillation similar to that observed in the experiments (figure 12). The pressure variation at the $r/R = 0.5$ check point illustrates the gradual development of the flow from a pulsation into an oscillation mode (figure 13).

Since for $L/D = 2.5$ the flow structure gradually changed from pulsation mode into oscillation mode, further computations were performed for $L/D = 2.0$. Computations using UUC were carried out for longer time and very small time steps to determine
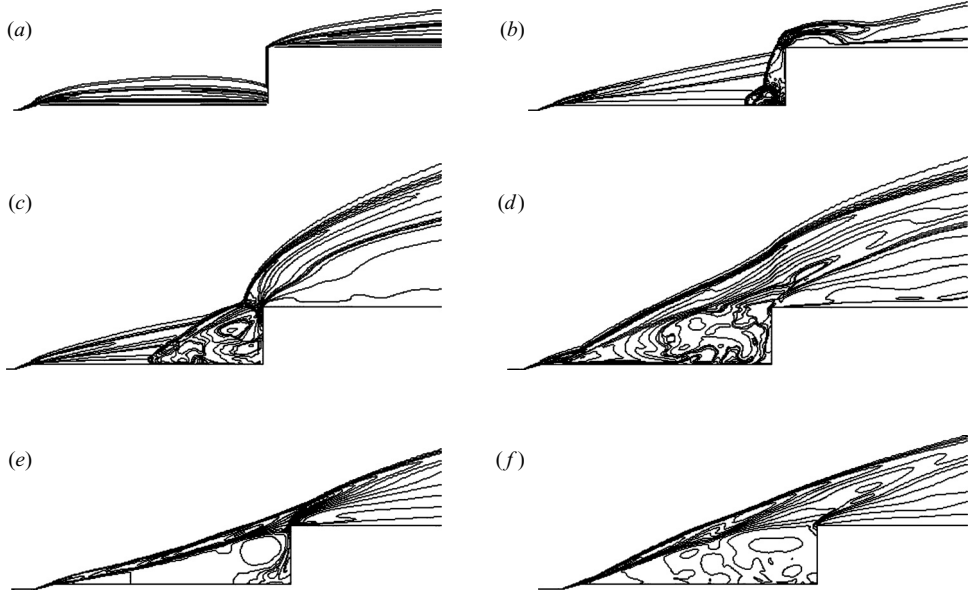
FIGURE 11. Spiked cylinder, $M = 6.0$, $L/D = 2.0$. Initial flow development obtained with the SFU procedure (use of steady solver).
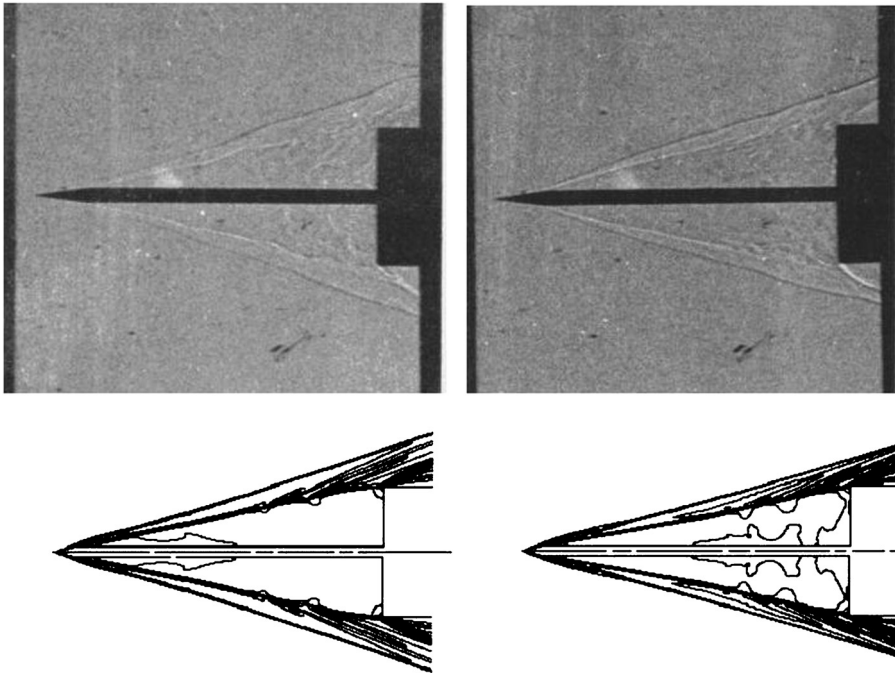

FIGURE 12. Spiked cylinder, $M = 6.0$, $L/D = 2.5$. Comparisons of present computations (lower) with experimental results (upper).

whether or not these factors affect the possible transition to an oscillation mode. The results shown in figures 14 and 15 confirmed that these factors did not have any effect. Furthermore, a near-wall grid-spacing refinement using the grid containing 147 439
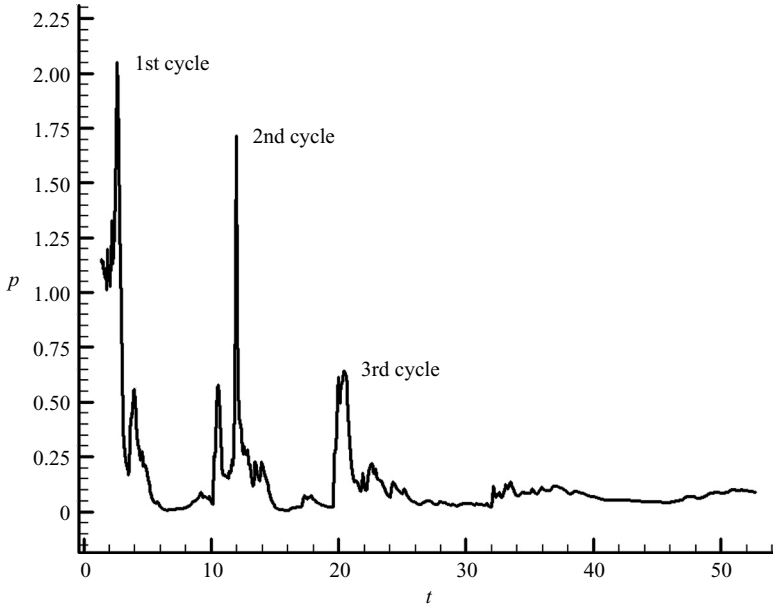
FIGURE 13. Spiked cylinder, $M = 6.0$, $L/D = 2.5$. Pressure variation at a point on the surface of the cylinder located at radial distance from the axis $r/R = 0.5$.
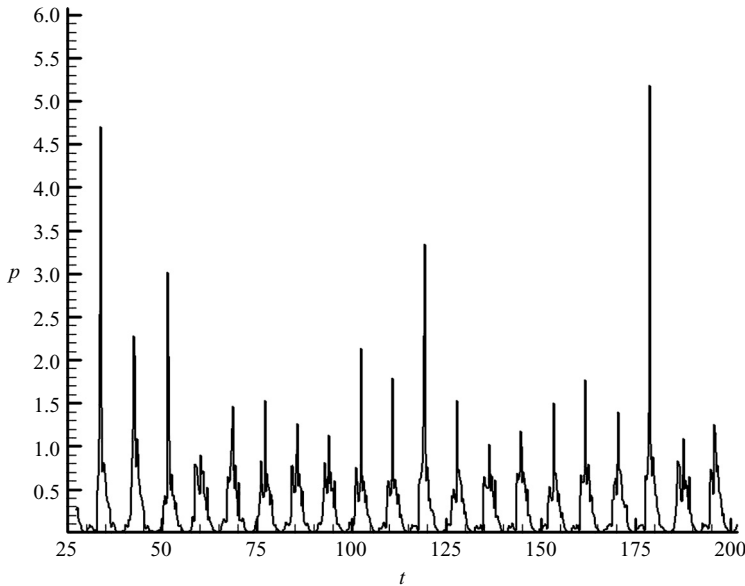

FIGURE 14. Spiked cylinder, $M = 6.0$, $L/D = 2.0$. Medium grid and long time run. Pressure is measured at a point on the surface of the cylinder located at radial distance $r/R = 0.5$ from the axis.

points and the first grid cell off the wall located at $10^{-4}D$ and $10^{-3}D$, respectively, showed that the results for the above grid spacing were identical.

The simulations of the VKI spiked cylinder experiments revealed the existence of a range of spike lengths, within which both modes of instability may appear, depending
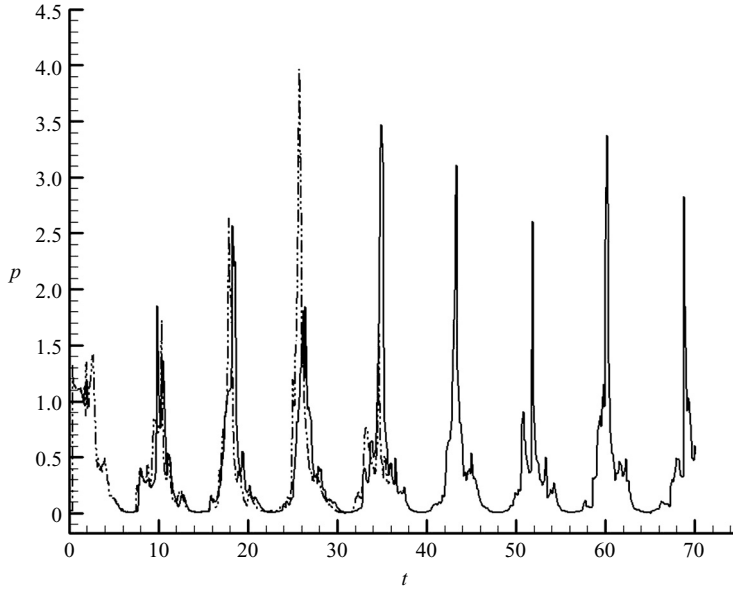
FIGURE 15. Spiked cylinder, $M = 6.0$, $L/D = 2.0$. Investigation of the effect of time step on pressure variation (computations performed on the fine grid); continuous line: $DT = 0.0005$; dashed-dot line: $DT = 0.00005$.

on the initial flow conditions. The hysteresis phenomenon has not been observed in the VKI experimental tests due to the discrete type of each wind tunnel run and it is not, therefore, certain that the double-solution limit coincides with the limits of hysteresis.

3.2. *Cone-frustum with retractable spike*

The second flow configuration is the $M = 3.0$, $Re = 3.94 \times 10^5$ flow around a cone frustrum axisymmetric model ($D = 56.39$ mm) equipped with a retractable spike for which experimental data have been documented by Calarese & Hankey (1985). The ability to extend or retract the spike during the experiment proved very beneficial for the investigation of the structure of the flow since it verified the existence of the hysteresis phenomenon.

The experiment showed that depending on the spike length, the flow may be steady or unsteady, resulting in either a stable or unstable shock structure. The stable shock configurations occur for small spike lengths, where the spike does not protrude from the bow shock, or for sufficiently large ones, signified by low levels of pressure fluctuation at pressure port locations on the cylinder surface. Within the unstable region (corresponding to spike length between $L = 13$ and 44 mm) the shock may oscillate axially in a symmetric or asymmetric fashion which also depends on the spike length. More particularly, the asymmetric oscillation appeared for spike length less that 35.56 mm. Note that the term 'oscillation' used by Calarese & Hankey (1985) corresponds to the term 'pulsation' used in the present study. Furthermore, the term 'stable shock structure' includes not only the case of steady flow, but also the 'oscillation' case (terminology of Kabelitz 1971).

Flow hysteresis (figure 4) is the most important finding of Calarese & Hankey (1985). Shang *et al.* (1980) have simulated very successfully the flow about this body, for spike length $L = 38.1$ mm ($L/D = 0.675$). The selected flow lies within the hysteresis
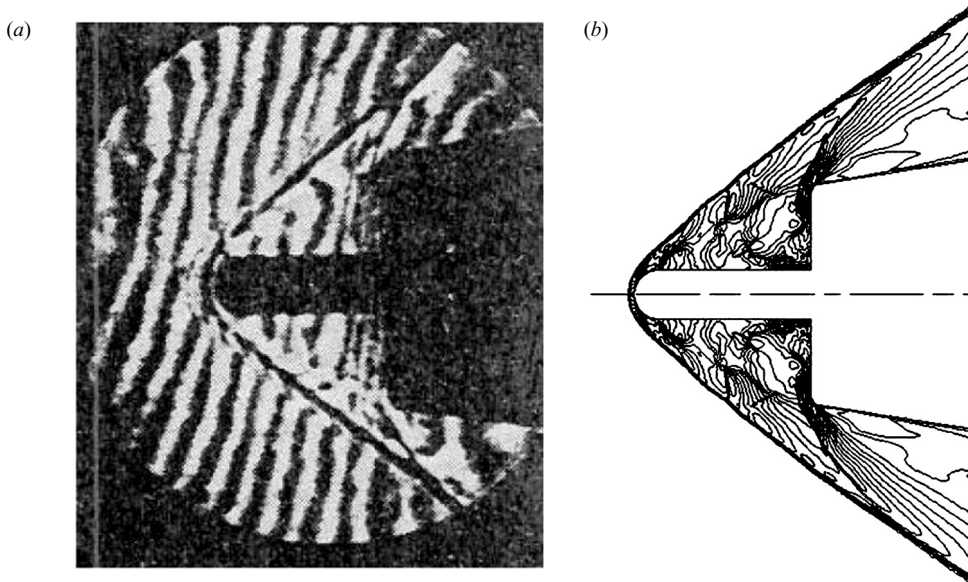
FIGURE 16. Spike-tipped body of Calarese & Hankey (1985), $M = 3.0$, $L/D = 0.8$;
(*a*) experimental results; (*b*) numerical solution using the SFU procedure.

region (figure 4). Similar to Shang *et al.* (1980), laminar flow and isothermal wall conditions ($T = 311°$K) were also employed in this study.

The present study investigates whether the bifurcation of a numerical solution persists outside the hysteresis region. Calarese & Hankey (1985) included in their paper the Schlieren picture shown in figure 16(*a*). It corresponds to spike length, $L/D = 0.8$ ($L = 45.2$ mm), and the shock envelope is steady. This spike length has been selected for simulation here ($L/D = 0.8$). A grid consisting of 146 275 points, distributed in five blocks, was considered as the basic one. Then a coarser grid of 37 000 points was generated, by taking every second point in each direction correspondingly. The SFU procedure predicted a stable solution (figure 16*b*), very similar to the experimental flow shown in figure 16(*a*). To the contrary, application of the UUC procedure to both grids predicted a pulsation mode (figure 17) instead of a stable flow. The periodicities of the solution and pressure amplitude were similarly obtained by the two grids (figure 18). Calculation of the error with respect to pressure peak positions and root-mean-square pressure amplitudes for different grid resolutions showed that when doubling the grid cells in each direction the error is confined within a 1 %–8 % (depending on the time instant taken for estimating the error with respect to the pressure peak position).

The inability of the UUC procedure to match the experimental behaviour is the most interesting finding of this simulation. The investigation reveals that in the numerical context the pulsation mode flow regime can persist outside the hysteresis region depending on the assumed initial flow conditions.

3.3. *Crawford's spiked hemisphere cylinder*

Crawford (1959) studied flow over a spiked-nose hemisphere–cylinder at $M = 6.8$, Reynolds numbers in the range of 1.2×10^5 to 1.5×10^6, and spike lengths in the range of $L/D = 0.5$–4.0. The experiments provided Schlieren images and pressure distributions along the hemisphere cylinder. According to Crawford (1959), the
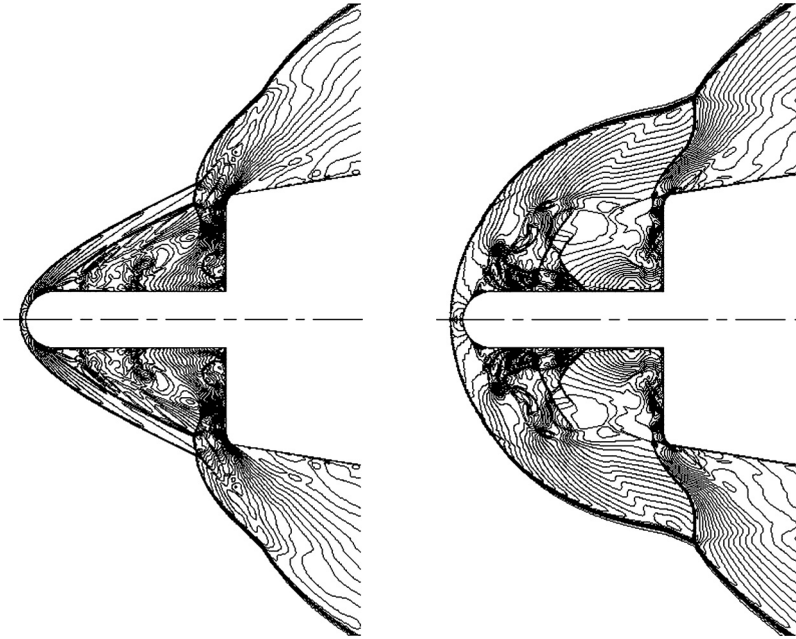
FIGURE 17. Spike-tipped body of Calarese & Hankey (1985), $M = 3.0$, $L/D = 0.8$. Computed density contours using free stream conditions and the UUC procedure.
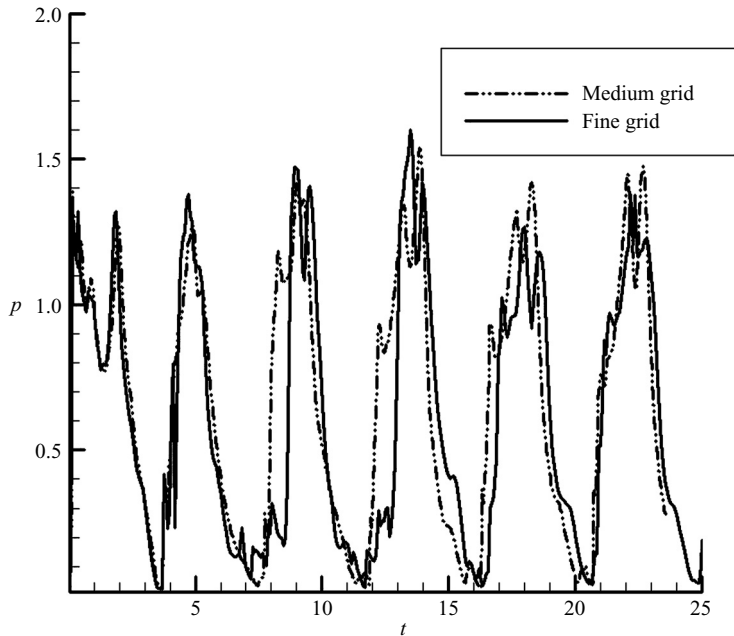

FIGURE 18. Spike-tipped body of Calarese & Hankey (1985), $M = 3.0$, $L/D = 0.8$. Effect of grid resolution on pressure variations at a point on the surface of the body located at radial distance from the axis $r/R = 0.40$.
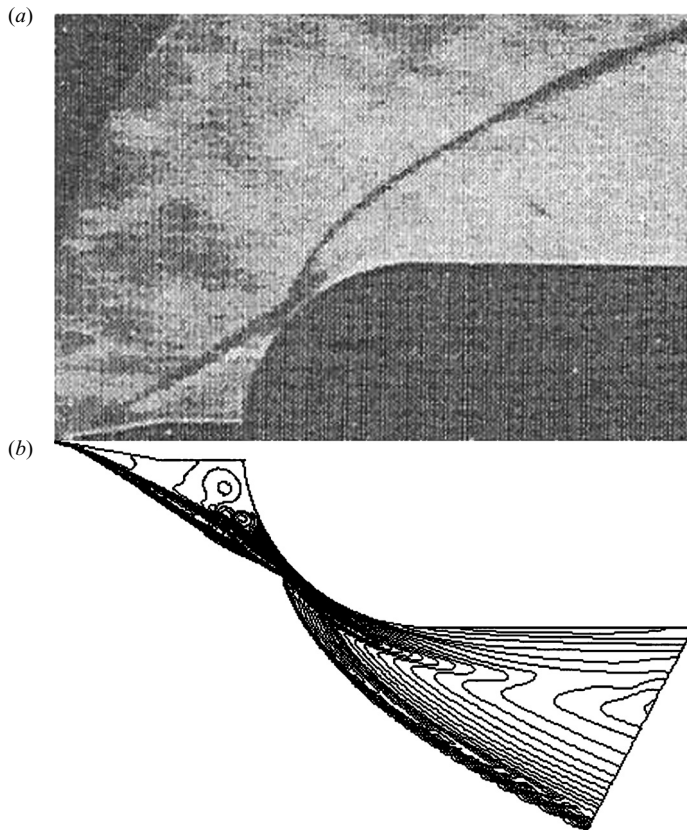
(a)

(b)

FIGURE 19. Crawford's spiked cylinder. Comparison of computation (*b*) and experiment (*a*) at $Re = 1.4 \times 10^5$.

Schlieren pictures of the separated flow over the spikes at the lowest Reynolds numbers (1.4×10^5 to 2.3×10^5) show little or no evidence of unsteady flow. As the Reynolds number increases, the initiation of turbulent transition moves the boundary of separation forward and there is some evidence of unsteady flow behaviour of small amplitude and high frequency without, however, affecting the shape of the separated region. At the lowest Reynolds numbers the flow remained laminar, although in some cases there was some evidence of transition at the location of reattachment. At Reynolds number approximately 3.0×10^5 the onset of transition was evident ahead of reattachment. Indirect evidence of the changing structure of the flow is provided by the measured pressure distributions, along the hemisphere cylinder. Indeed, in the related figure in Crawford's report, the Reynolds number covers the range: 1.2×10^5 to 1.3×10^6. The value of the pressure at each measuring port along the hemisphere depends on the particular Reynolds number of the run.

For the purpose of the present investigation, it was sufficient to consider only the shortest spike configuration ($L/D = 0.5$), thereby avoiding the complexities associated with the transitional and turbulent flow regimes. The laminar flow cases correspond to $L/D = 0.5$, and include $Re = 1.4 \times 10^5$ and $Re = 2.3 \times 10^5$. Calculations were performed for both Reynolds numbers and compared with the Schlieren picture (for $L/D = 0.5$ and $Re = 1.4 \times 10^5$) and pressure distributions (for $Re = 2.3 \times 10^5$) provided in Crawford's report.
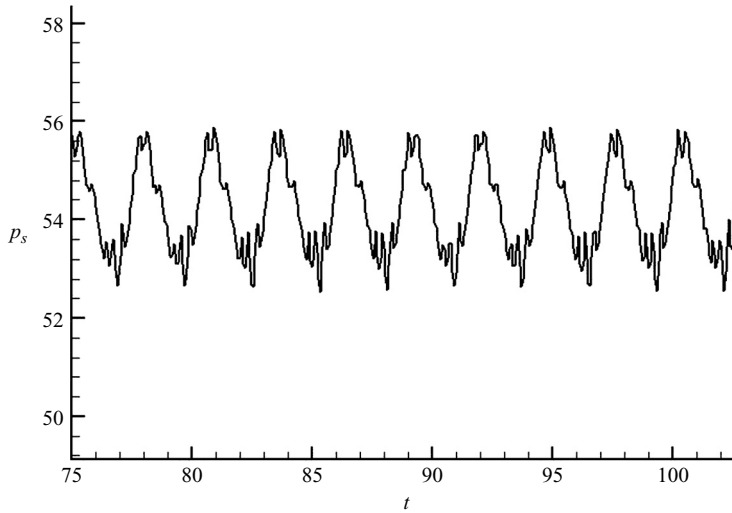
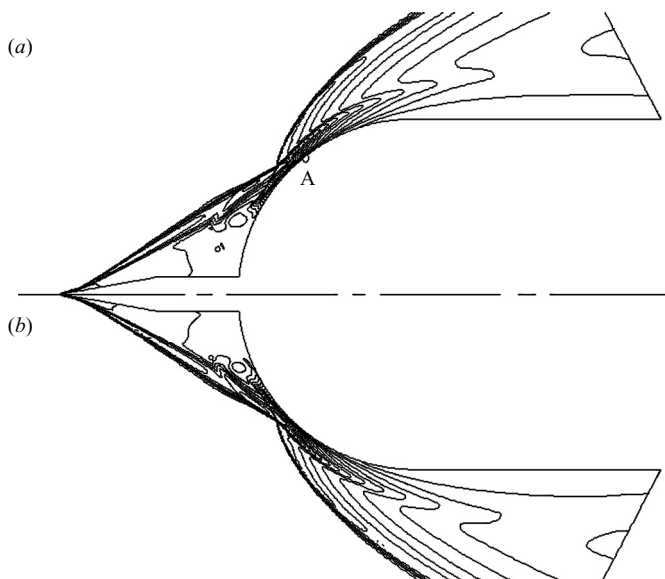FIGURE 20. Crawford's spiked cylinder, $Re = 1.4 \times 10^5$. Pressure variation.

FIGURE 21. Crawford's spiked cylinder. Density contours variation during an oscillation cycle, $Re = 1.4 \times 10^5$. (*a*) When pressure is maximum at point A. (*b*) When pressure is minimum at point A.

The simulations were performed using both the UUC and the SFU procedure. A computational gird containing 393×131 grid points in the streamwise and wall normal directions, respectively, was employed. Starting with the lower Reynolds number test case ($Re = 1.4 \times 10^5$), the computed density contours are shown in figure 19, along with the experimental picture, revealing good qualitative agreement between experiment and simulation. The pressure variation shown in figure 20, at a
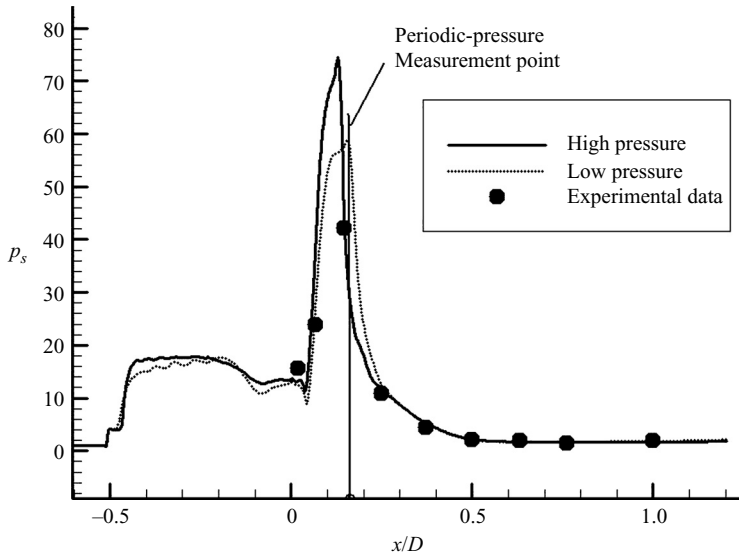
FIGURE 22. Comparison of computed pressure distributions with experimental data of Crawford at $Re = 2.3 \times 10^5$.
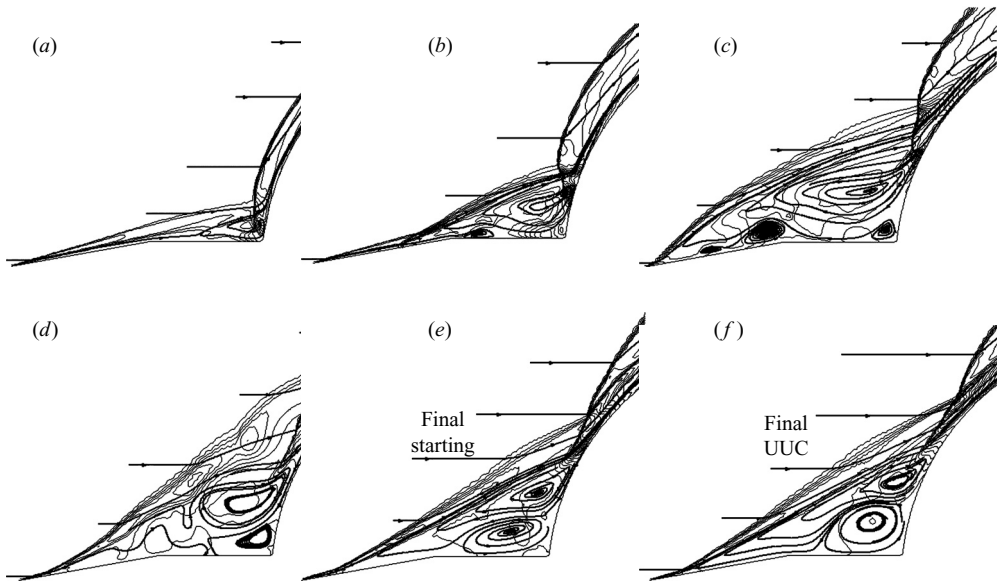

FIGURE 23. Initial phase of flow simulation of Crawford's test case. Application of UUC calculation procedure.

point in the region of reattachment of the conical shear layer (point A in figure 21), indicated a self-sustained oscillation of small pressure amplitude ($\sim 5.5\%$). Mehta (2002), also, found that the same flow is characterized by a self-sustained oscillation. Interestingly, visualization of the conical shear layer and the shock system using density contours, at the two extreme values of pressure at point A, shows a steady
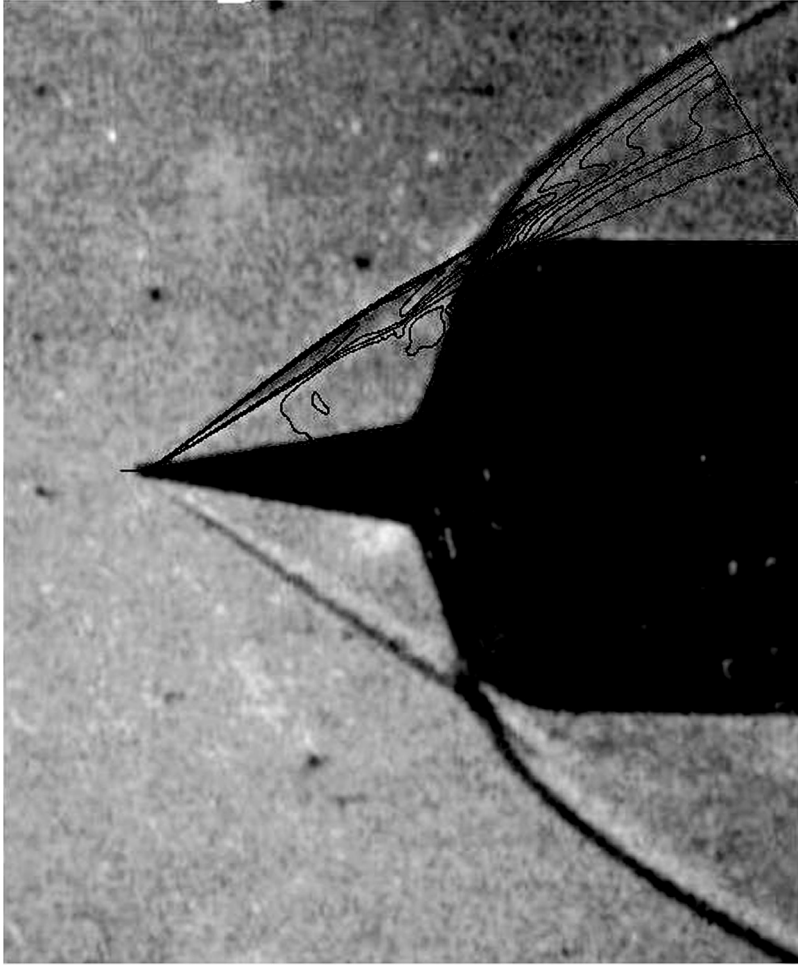
FIGURE 24. Comparison of results (solid lines) with the SFU procedure and Panaras's experiment (Schlieren) for Conic 1 body.

structure with no evidence of oscillation (figure 21). The symbol p_s in figures 20 and 22 denotes local pressure non-dimensionalized by free stream pressure.

The $Re = 2.3 \times 10^5$ case was also simulated, since experimental data for the surface pressure distribution are available. As the Reynolds number increased, the amplitude of the self-sustained pressure oscillations increased by an order of magnitude. This behaviour agrees with the observations of Crawford according to which as the Reynolds number increases, there is evidence of unsteady flow of small amplitude and high frequency. The computed pressure distribution along the hemisphere–cylinder is compared with the experimental data in figure 22. There are two sets of pressure data in figure 22, corresponding to the periodic pressure minima and maxima. Note that according to Crawford '*no effect of the oscillation of the separated boundaries and shocks was noticed in the pressure measurements; probably the frequency of oscillation was too high for the frequency response of the pressure-measurement instruments*'.
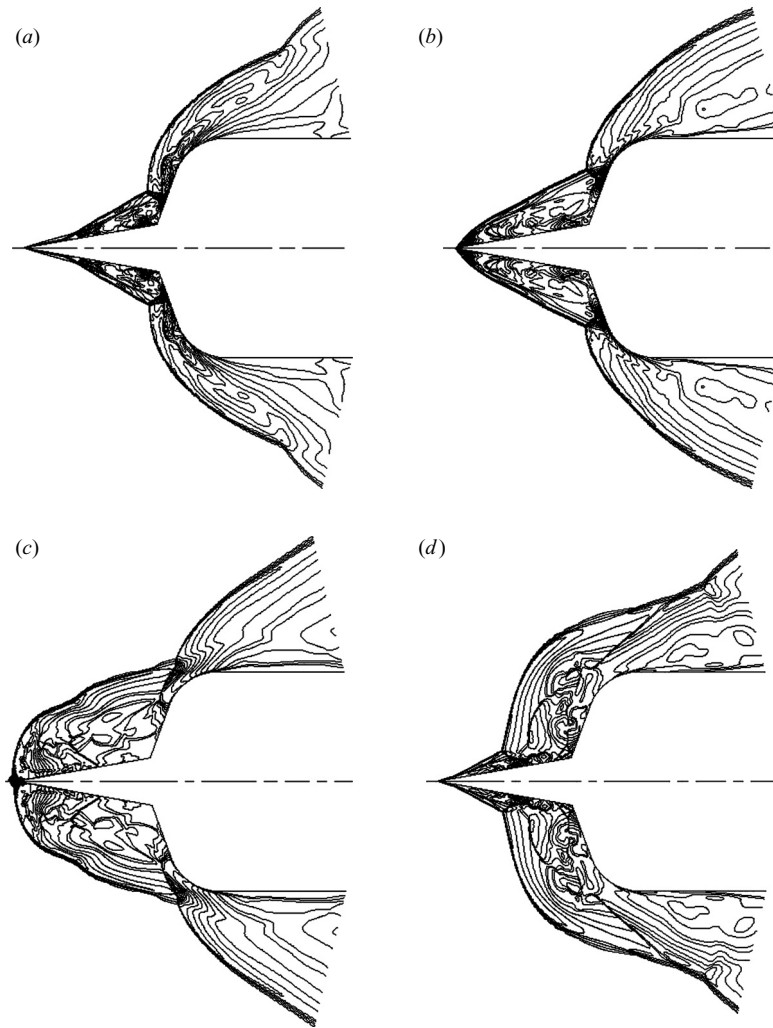
FIGURE 25. Results for the Conic 1 case using the UUC procedure.

The early stages of flow development as predicted by the UUC procedure is shown in figure 23, for the $Re = 1.4 \times 10^5$ test case. The conical separation bubble grows laterally (figures 23a–23d), reaches the expansion part of the afterbody and, subsequently, the air escapes downstream, leading to the establishment of an attached conical separation bubble (figure 23e). The flow changed very little at later times (figure 23f). The SFU procedure provided identical results. Thus, in the present case, where the simulated flow is stable, there is no effect of the flow initialization on the numerically predicted results. Therefore, it appears that numerical instability arising from the use of different flow initializations is intimately linked to the physics of the flow. To further examine the effects of flow initialization on the stable high-speed flows, two conic body cases are discussed in the next section.

3.4. *Concave conic bodies*

The final flow configurations concern two optimized conic bodies (Panaras 1976), referred to as 'Conic 1' and 'Conic 2'. Conic 1 has cone angles $10°/70°$ and radius
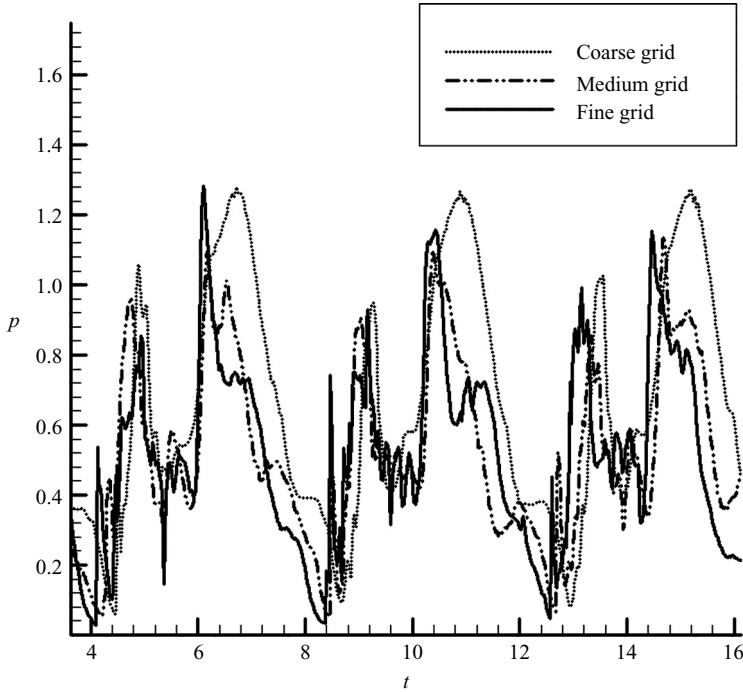
FIGURE 26. Panaras (1976) Conic 1 body ($M = 6.0$). Effect of grid resolution on pressure variations at a point on the surface of the afterbody located at radial distance from the axis $r/R = 0.39$.

of curvature at the shoulder of the second cone $r = 0.2D$. It has been experimentally tested at $M = 6.0$ and $Re = 1.2 \times 10^5$. The Schlieren images indicate that a steady shock system envelops the forebody and attaches on the rounded shoulder of the afterbody (figure 24). Figure 24 compares the density contours obtained using the SFU procedure (on a grid containing 223 811 points) with the Schlieren images, showing very good agreement.

To the contrary, the results obtained with the UUC procedure demonstrate a well-established pulsation cycle of instability (figure 25). This was verified by using three different grids consisting of 223 811, 58 750 and 14 805 points labelled as 'fine', 'medium' and 'coarse' grids, respectively. The medium and coarse grids were generated, by taking every second and every fourth point in each direction, correspondingly, of the fine grid. Application of the UUC procedure (unsteady uniform conditions) employing the three grids led to the same flow prediction , i.e. pulsating flow, contrary to the steady solution revealed by the experiment. The results for pressure time history at the $r/R = 0.39$ point of the aftercone are shown in figure 26. The solutions obtained from the 'medium' and 'fine' grids are comparable with respect to time periodicity and amplitude of pressure variation. Note that this is a much tougher case with respect to grid convergence. Calculation of the error with respect to pressure peak positions and root-mean-square pressure amplitudes for different grid resolutions showed that when doubling the grid cells in each direction the error is confined within 1 %–8 % (depending on the time instant taken for estimating the error with respect to the pressure peak position).
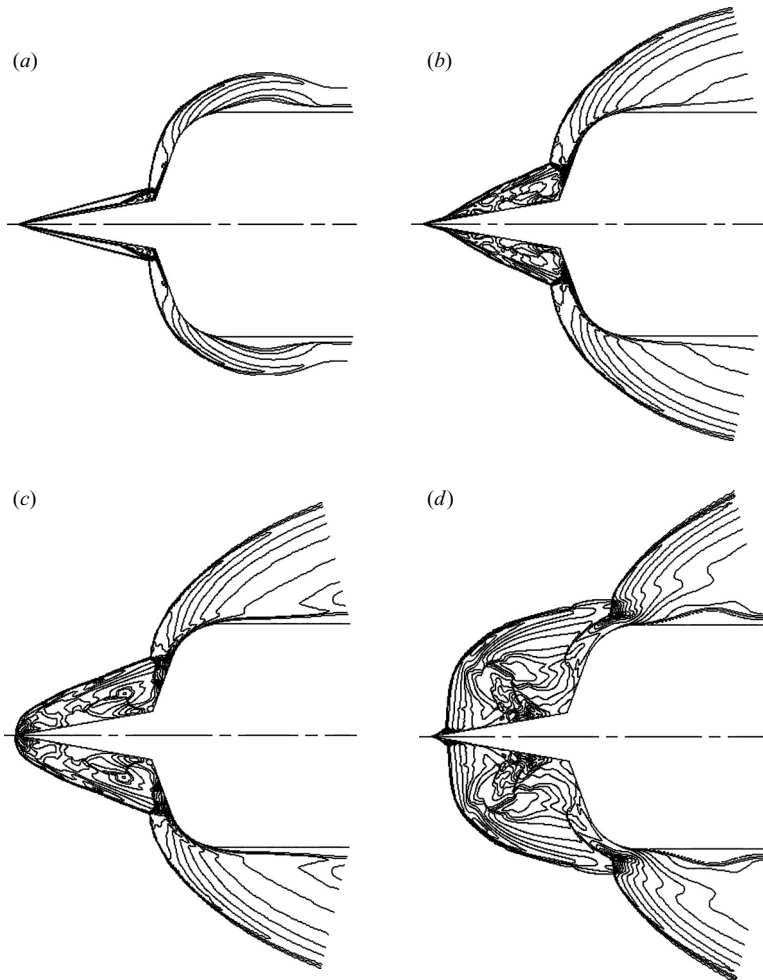
FIGURE 27. Early stages of the flow field obtained with the UUC procedure for Conic 1 (application of the unsteady solver).

The initial flow development (figures 27*a* and 28*a*) is similarly predicted by the UUC and SFU procedures. However, the UUC procedure results in the growth of the conical separation bubble which reaches the leading edge of the forecone before reaching the rounded shoulder of the aftercone (figures 27*b* and 27*c*). Then, the separation bubble inflates radially to a non-equilibrium state (figure 27*d*), i.e. a prelude for the subsequent collapse of the bubble and the establishment of conditions similar to those shown in figure 25.

Using the SFU procedure, the flow develops with higher rate in the radial direction than in the axial one. Thus, when the growing separation bubble reaches the shoulder of the aftercone its upstream front is far from the leading edge of the forecone (figure 28*b*). Subsequently, it envelops the shoulder and the excess air escapes downstream (figure 28*c*). The SFU procedure provides the stable flow shown in figure 24.

The Conic 2 body has cone angles $20°/70°$ and radius of curvature at the shoulder of the second cone $r = 0.2D$ and the experiments have been conducted at the same
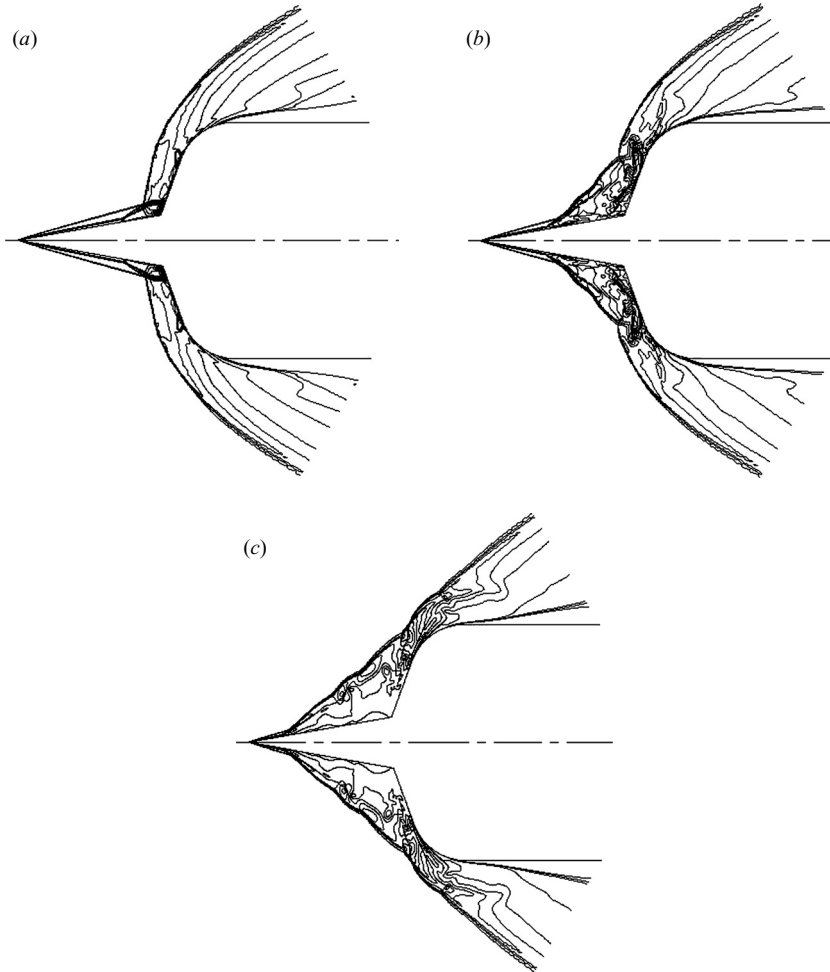
FIGURE 28. Early stages of the flow field obtained with the SFU procedure for Conic 1 (application of the steady solver).

Mach and Reynolds numbers as for Conic 1. The computational grid contained 223 811 points. For this case, both the UUC and SFU provided physically correct solutions. The early stages of the flow development (figure 29) indicate that due to the large length of the forecone, the growing conical separation bubble reaches the shoulder of the aftercone, before reaching the tip of the conic forecone (figure 29*c*). Its subsequent inflation is mild, since the excess air escapes downstream (figure 29*d*). Then, the flow stabilizes to the steady solution of figure 29(*e*), which is very close to the experiment (figure 30).

4. Concluding remarks

Classical experimental studies of flows around spiked-blunt bodies have shown that if the geometry of a blunt body is such that a detached bow shock appears, then if the spike is sufficiently long to protrude from the bow shock, the resulting foreshock–aftershock interaction may lead to unsteady flow. This unsteady flow is characterized
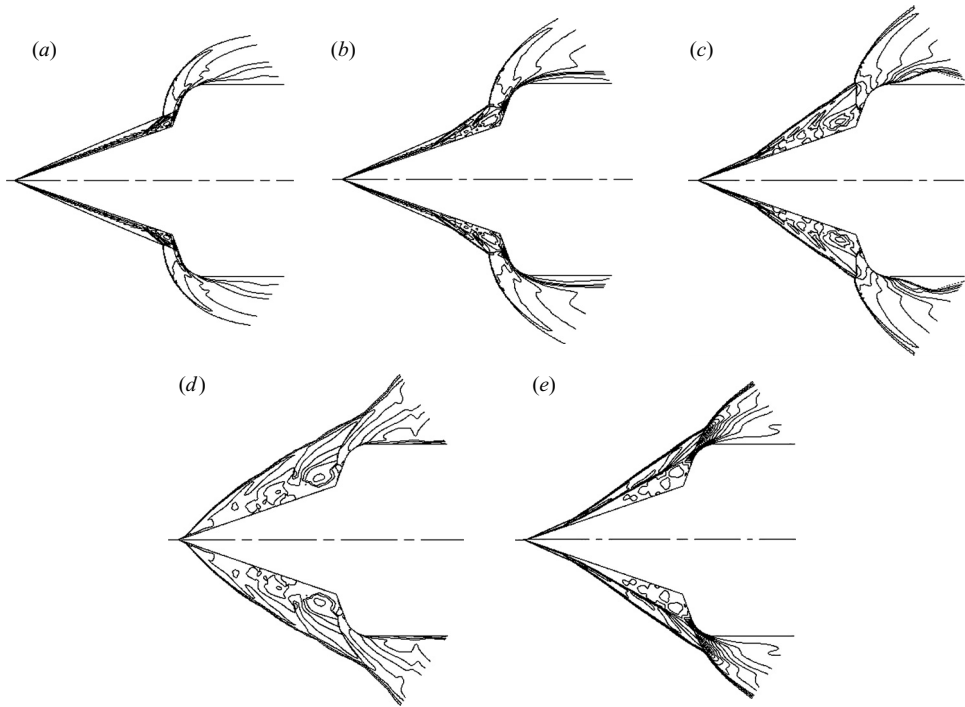
FIGURE 29. Early stages of the flow field obtained with the UUC procedure for Conic 2.

by periodic radial inflation of the conical separation bubble which is formed around the forebody. Since there is no disturbance to sustain the hemispherical bubble around the tip of the forebody, it collapses downstream leading to appearance of free stream conditions in the majority of the flow field, and hence repetition of the cycle of instability, known as pulsation mode. When the spike length increases, the pulsation persists reaching a limit beyond which the flow unsteadiness is abruptly transformed into the oscillation mode. The oscillation is characterized by a mild radial oscillation of the conically shaped shock system and the accompanied shear layer. When the spike length changes during a wind tunnel test, hysteresis is also observed, i.e. the flow retains its previous state, although depending on the spike length, the instability mode may change from pulsation to oscillation or vice versa.

The present study examined the effect of flow initialization on the numerical prediction of the above flows. Direct application of a time-accurate (unsteady) procedure in conjunction with uniform free stream conditions (UUC procedure) provided, in some cases, persisting non-physical pulsation mode, contrary to experimental evidence that shows mild oscillating or almost steady flow, i.e. exhibiting oscillations of very small amplitude in the reattaching part of the flow. On the other hand, initiation of time-accurate computations using an initial flow condition based on an approximate steady-state (non-uniform) flow (SFU procedure) provided the experimentally observed flow behaviour.

Detailed examination of the transient flow development for the various cases considered here revealed that at the early stages of flow development, as well as depending on the geometry details, both initialization procedures predict an almost inviscid flow field characterized by a foreshock–aftershock interaction. The shock
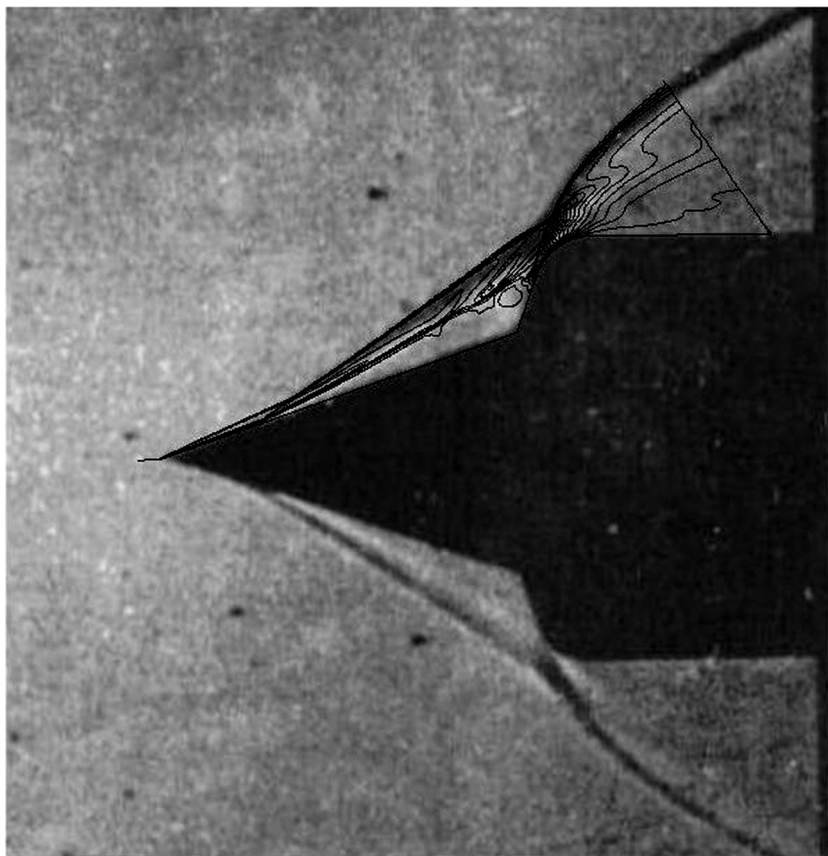
Figure 30. Comparison of computation with experiment for Conic 2.

formation is similar to the shock pattern IV of Edney, which is characterised by the appearance of a supersonic jet impinging on the surface of the body, separating the high-pressure region behind the strong bow shock from the low pressure within the grownconical separation bubble. Subsequently, the separation bubble is formed and grows. If the flow is pulsating, the transient flow development is not sensitive to the initial condition.

When the flow is oscillating or almost steady, the transient flow development as obtained by the SFU procedure leads to the correct flow development, whereas the UUC procedure is likely to lead to an erroneous pulsating flow. Although observation of the transient flow development provides valuable insight into the effects of geometry and initial flow condition on the numerical simulation, it is not presently possible to set up *quantitative* rules for an *a priori* judgement of these effects on unstable supersonic and hypersonic flows.

Aerothermodynamic Flight Prediction Tools". Part of the present work originated within the framework of this Group.

Appendix. Governing equations

The governing equations in axisymmetric and differential form for an arbitrary control volume are written as

$$r \frac{\partial U}{\partial t} + \nabla \cdot ((H_c - H_v)r) = S.$$

Here U represents the conserved variables, while H_c and H_v represent the convective and viscous fluxes, respectively. Axisymmetric source terms here appear as S while the radius r is also involved. The fluxes are written as

$$U = \begin{bmatrix} \rho \\ \rho u_r \\ \rho u_z \\ \rho e \end{bmatrix} \quad H_c = \begin{bmatrix} \rho u_r & \rho u_z \\ \rho u_r^2 + p & \rho u_r u_z \\ \rho u_r u_z & \rho u_z^2 + p \\ u_r(\rho e + p) & u_z(\rho e + p) \end{bmatrix}$$

$$H_v = - \begin{bmatrix} 0 & 0 \\ \tau_{rr} & \tau_{rz} \\ \tau_{zr} & \tau_{zz} \\ u_r\tau_{rr} + u_z\tau_{rz} + q_r & u_r\tau_{zr} + u_z\tau_{zz} + qz \end{bmatrix},$$

and $S = (0, S_r, S_z, S_E)^\mathrm{T}$ where

$$S_r = p - \tau_{\theta\theta} - \frac{2}{3} \frac{\partial(\mu u_r)}{\partial r},$$

$$S_z = -\frac{2}{3} \frac{\partial(\mu u_r)}{\partial z},$$

$$S_E = \frac{2}{3}\mu \left(\frac{u_r^2}{r} \right) + r \left(\frac{\partial}{\partial r} \left(\frac{2}{3}\mu \frac{u_r^2}{r} \right) + \frac{\partial}{\partial z} \left(\frac{2}{3}\mu \frac{u_z u_r}{r} \right) \right),$$

and τ_{kl} (k, l stand for r, θ, z), q and μ are the viscous stresses, heat fluxes and the viscosity coefficient, respectively. The perfect gas equation of state, $p = \rho(\gamma - 1)i$, is employed to calculate pressure p and the value of γ is taken as a constant equal to 1.4. For the present geometries, the equations are transformed in body-fitted curvilinear grid co-ordinates (Drikakis & Rider 2005; and reference therein).

REFERENCES

BATCHELOR, G. K. 2000 *An Introduction to Fluid Dynamics*. Cambridge University Press.

CALARESE, W. & HANKEY, W. L. 1985 Modes of shock-wave oscillations on spike-tipped bodies. *AIAA J.* **23**, 185–192.

CRAWFORD, D. H. 1959 Investigation of the flow over a spiked-nose hemisphere-cylinder at a Mach number of 6.8. *NASA* D-118.

DRIKAKIS, D. & RIDER, W. 2005 *High-Resolution Methods for Incompressible and Low-Speed Flows*. Springer.

DRIKAKIS, D. & SMOLARKIEWICZ, P. K. 2001 On spurious vortical structures. *J. Comput. Phys.* **172**, 309–325.

EDNEY, D. 1968 Anomalous heat transfer and pressure distributions on blunt bodies at hypersonic speeds in the presence of an impinging shock. *FFA* Rep. 115.

FESZTY, D., BADCOCK, K. J. & RICHARDS, B. E. 2004a Driving mechanisms of high-speed unsteady spiked body flows. Part 1. Pulsation mode. *AIAA J.* **42**, 95–106.

Feszty, D., Badcock, K. J. & Richards, B. E. 2004b 'Driving mechanisms of high-speed unsteady spiked body flows. Part 2. Oscillation mode. *AIAA J.* **42**, 107–113.

Holden, M. S., Wandhams, T. P., Harvey, J. K. & Candler, G. V. 2002 Comparisons between DSMC and Navier–Stokes solutions and measurements in regions of laminar shock wave boundary layer interaction in hypersonic flows. *AIAA Paper* 2002–0435.

Kabelitz, H. 1971 Zur Stabilitaet geschlossener Grenzschichtabloese-gebiete an konischen Drenkoerpern bei Hyperschallaus-stroemung. *DLR* FB 71–77.

Kenworthy, M. 1978 A study of unstable axisymmetric separation in high speed flows. Ph.D. Dissertation, Department of Aerospace and Ocean Engineering, Virginia Polytechnic Institute And State University, Blacksburg, VA, USA.

Mair, W. 1952 Experiments on separated boundary layers on probes in front of blunt nosed bodies in a supersonic air stream. *Phil. Mag.* **43**, 695–716.

Maull, D. 1962 Hypersonic flow over axially symmetric spiked bodies. *J. Fluid Mech.* **12**, 614–624.

Mehta, R. C. 2002 Numerical analysis of pressure oscillations over axisymmetric spiked blunt bodies at Mach 6.80. *Shock Waves* **11**, 431–440.

Morrison, J. H. 1992 A compressible Navier–Stokes solver with two-equation and Reynolds stress turbulence closure models. *NASA* CR-4440.

Panaras, A. G. 1976 The high speed unsteady separation around concave bodies can be explained by an inviscid flow mechanism. These Annexe, *VKI-Free University of Brussels*.

Panaras, A. G. 1977 High speed unsteady separation about concave bodies – A physical explanation, von Karman Institute, *Tech. Note* 123.

Panaras A. G. 1981 Pulsating flows about axisymmetric concave bodies. *AIAA J.* **9**, 804–806.

Panaras, A. G. 1985 Pressure pulses generated by the interaction of discrete vortices with an edge. *J. Fluid Mech.* **154**, 445–462.

Roe, P. L. 1981 Approximate Riemann solvers, parameter vectors, and difference schemes. *J. Comp. Phys.* **43**, 357–372.

Rumsey, C. L., Sanetrik, M. D., Biedron, R. T., Melson, N. D. & Parlette, E. B. 1996 Efficiency and accuracy of time-accurate turbulent Navier–Stokes computations. *Comput. Fluids.* **25** (2), 217–236.

Schramm, J. M. & Eitelberg, G 1999 Shock boundary layer interaction in hypersonic high enthalpy flow on a double wedge, Paper 5150, *22nd International Symposium on Shock Waves*, Imperial College, London, UK, July 18–23.

Shang. J. S., Hankey, W. L. & Smith, R. E. 1980 Flow oscillations of spike-tipped bodies. *AIAA Paper* 80-0062.

Van Leer, B. 1979 Towards the ultimate conservative difference scheme V. A second order Sequel to Godunov's method. *J. Comp. Phys.* **32**, 101–136.

Wood, C. 1960 Experimental flow over spiked flows. *J. Fluid Mech.* **8** 584–594.

Yee, H. C. 2001 Building block for reliable non-linear numerical simulations. In *Turbulent Flow Computation* (Ed. D. Drikakis & B. Geurts). Kluwer Academic Publisher.